NRC Research Press

ARTICLE

Removing residual airborne sensor motion for measuring seismic signals from a drone

Thomas Rapstine and Paul Sava

Abstract: Acquiring seismic data using drones requires excellent knowledge of the drone's motion since positional measurements made from an airborne sensor represent a combination of sensor and ground motion. Recent advancements in laser Doppler vibrometry and repeat lidar surveys show that the frequency and resolution of non-contact motion measurements is increasing to the point necessary for measuring seismic signals. We explore the conditions under which separation of sensor motion from ground motion can be accomplished in practice. We assume (*i*) that the translation and rotation of a stabilized airborne sensor follows an analytic form in time that is either known or can be estimated from the sensor's measurements, (*ii*) that the seismic signal we observe has compact support contained within the measurement window, and (*iii*) that the ground motion can be described by a rigid translation. We analyze the effectiveness of our signal separation problem as a function of peak signal, sensor noise level, sensor rotation angle, and sensor point sampling density by defining a boundary where SNR = 0 dB for various combinations of these parameters. We find that under the set of assumptions, lower rotation angles, lower sensor noise, and denser point samplings on the ground provide better signal separation using our method.

Key words: airborne, seismic, signal separation, simulation.

Résumé : L'acquisition de données sismiques à partir de drones nécessite une excellente connaissance du mouvement du drone, car les mesures de position effectuées à partir d'un détecteur aérien représentent une combinaison de mouvement du détecteur et du sol. Des progrès récents dans la vibrométrie Doppler à laser et les levés lidar répétés montrent que la fréquence et la résolution des mesures de mouvement sans contact augmentent au point essentiel pour mesurer les signaux sismiques. Les auteurs explorent les conditions dans lesquelles la séparation entre le mouvement du détecteur et le mouvement du sol peut être réalisée dans la pratique. Ils supposent (*i*) que la translation et la rotation d'un détecteur aérien stabilisé suivent une forme analytique dans le temps qui est connue ou qui peut être estimée à partir des mesures du détecteur, (*ii*) que le signal sismique observé a un support compact circonscrit dans la fenêtre de mesure, et (*iii*) que le mouvement du sol peut être décrit par une translation rigide. Ils analysent l'efficacité de leur problème de séparation du signal en fonction du signal de crête, du niveau de bruit du détecteur, de l'angle de rotation du détecteur et de la densité d'échantillonnage de points du détecteur en définissant une limite où le rapport signal sur bruit SNR = 0 dB pour diverses combinaisons de ces paramètres. Ils constatent que, selon l'ensemble des hypothèses, des angles de rotation plus faibles, un bruit de détecteur plus faible et des échantillonnages de points plus denses au sol offrent une meilleure séparation des signaux en utilisant leur méthode. [Traduit par la Rédaction]

Received 28 April 2020. Accepted 3 May 2021.

T. Rapstine and P. Sava. Center for Wave Phenomena and Dept. of Geophysics, Colorado School of Mines, Golden, CO 80401, USA.
Corresponding author: Thomas Rapstine (e-mail: trapstin@mines.edu).
Copyright remains with the author(s) or their institution(s). Permission for reuse (free in most cases) can be obtained from copyright.com.

J. Unmanned Veh. Sys. Downloaded from cdnsciencepub.com by Thomas Rapstine on 12/16/21
For personal use only.

Mots-clés : aéroporté, sismique, séparation des signaux, simulation.

J. Unmanned Veh. Sys. Downloaded from cdnsciencepub.com by Thomas Rapstine on 12/16/21
For personal use only.

1. Introduction

The ability to gather seismic data from a drone would open new opportunities in seismology and seismic exploration. The range of ground displacement amplitude measurements for seismology and seismic exploration spans orders of magnitude, from sub-micron to centimetre amplitudes (Shearer 2005). Typical shot records recorded in land seismic applications have a duration of several seconds, while earthquake signals can have much longer durations, exceeding minutes (Center for Engineering Strong Motion Data 2016). Modern active seismic surveys require large arrays of geophones that must be physically placed in the ground to interrogate the subsurface. Consequently, deploying geophone arrays for exploration involves a large amount of equipment, personnel, and time; all of which compound into large acquisition costs. Airborne surveys using a fleet of drones could be faster, less environmentally impactful, and cheaper than current terrestrial alternatives. Drones have the advantage of being programmable, which would make for highly optimized and repeatable surveys of complex geometry. However, airborne seismic acquisition requires removing the negative effects of sensor motion from the measurements (Dräbenstedt et al. 2016; Rapstine et al. 2017). In this work, we use the term sensor motion defined as the motion an airborne sensor undergoes after a stabilization system, such as a gimbal, attempts to keep the sensor stationary. Previous virtual simulations have shown that modest airborne stereo video systems would be capable of measuring 1D displacements less than a few millimetres from a height of a few metres, provided the aircraft position and orientation are precisely known (Rapstine and Sava 2017; Rapstine et al. 2017). However, in reality the exact position of an airborne sensor is not known with arbitrary accuracy. In addition, measurement of 3D ground displacement would be desirable for seismic measurement, since motion due to seismic wave propagation is inherently 3D.

Here, we avoid the requirement to know the airborne sensor motion precisely, and instead establish a method for removing sensor motion that remains after the sensor is stabilized to recover the 3D displacement of the ground. We test the method in a virtual simulation to identify the conditions under which airborne seismic measurements are achievable in practice. Our method is appropriate for active seismic surveys where the source location and timing are known. We are inspired by recent successful applications remotely measuring seismic signals using laser Doppler vibrometer (LDV) systems (e.g., Dräbenstedt et al. 2016) and by the demonstrated sensitivity of high-speed video to subtle vibrations (e.g., Shahadi et al. 2020), which we summarize next.

Much progress has been made recently in proving the feasibility of LDV-based seismic measurements from stationary, mobile, airborne, and even space-borne platforms. The feasibility of remotely detecting ground motion caused by seismic waves was proven successful from a stationary platform positioned 800 m away from a vibrating target of interest (Berni 1991, 1994). More recently, work by Dräbenstedt et al. (2016) shows that a closer, yet mobile, LDV system equipped with a vibration isolation system can enable remote seismic measurements from a terrestrial vehicle, even in a windy acquisition environment. We note that Dräbenstedt et al. (2016) alludes to extending LDV-based seismic measurements to airborne platforms, but they cite a need for better clock synchronization, sensor vibration isolation, and methods for removing residual motion measured by a reference sensor before doing so. The effect a moving platform has on LDV measurements including the so-called “speckle noise” may be addressed by multiple independent LDV

J. Unmanned Veh. Sys. Downloaded from cdnsciencepub.com by Thomas Rapstine on 12/16/21
For personal use only.

sensors and signal processing algorithms, such as maximal ratio combining (Dräbenstedt 2014; Rembe and Dräbenstedt 2015; Courville and Sava 2019; Courville 2019). Maximal ratio combining leverages an assumption of independence between the LDV signals and the physics of speckle noise to enable measuring signals hidden by noise induced from a moving platform and the speckle pattern. This concept has been explored and analyzed even for satellite-borne LDVs in the context of conducting seismic surveys on asteriods or comets (Courville 2019). Whether on land, air, or in space an LDV still measures velocity at a single point whereas a distributed measurement of motion, in the form of displacement, may be available from video cameras.

High-speed cameras have been shown to successfully measure minute vibrations that cause changes in color. A technique known as motion magnification enables measuring subtle vibration using high-speed video by isolating spatiotemporal changes at specified image scales and frequencies (Wahbeh et al. 2003; Rubinstein and others 2014; Wadhwa et al. 2014; Wu et al. 2019; Shahadi et al. 2020). Motion magnification has successfully been used in a variety of applications including inferring structural composition from high-speed video (Chen et al. 2014), deducing vibrational modes of a structure (Shariati et al. 2015), measuring heartbeats (Wu et al. 2012), and recording audible speech by filming a vibrating object (Davis et al. 2014). However, motion magnification does not quantify the amplitude of motion we seek when recording seismic data, and only measures variations in color. Another technique, repeat lidar, does allow for the amplitude of motion to be quantified, which is required when conducting a seismic survey.

Repeat lidar enables non-contact measurements of ground displacement, which may improve in accuracy to a point that allows seismic signal measurement. Lidar technology has improved over recent years and is currently being used to measure large-scale geomorphic changes at the Earth's surface, for example, due to a landslide or debris-flow. Geomorphic changes are being measured via repeat lidar at increasingly higher frequencies from years (O'Neal and Pizzuto 2011; Neugirg et al. 2016) to months (Rabatel et al. 2008; Rengers and Tucker 2015; Longoni et al. 2016) to hours (Williams et al. 2018, 2019) and even to sub-second intervals in controlled large-scale laboratory settings (Rengers et al. 2019, 2020). Given recent advancements in LDV, high-speed video, and lidar technologies, we anticipate that a non-contact airborne sensor will soon be developed with the ability to measure a dense array of points on the ground with the accuracy necessary for seismic exploration. However, the problem of removing sensor motion from airborne measurements would remain and provides motivation for the work we present here.

We establish a signal separation technique that removes the negative effects of sensor motion after attempted hardware sensor stabilization (e.g., a gimbal). We construct our solution under assumptions appropriate for an active seismic survey, where seismic signals are only a few seconds long at most and are caused by a vibroseis or explosive source. Our technique works under a set of assumptions relevant for an airborne sensor that has been largely stabilized, but still experiences motion. We require an airborne sensor system that repeatedly measures the position of points on the ground as a function of time. Along with ground displacement, our method provides an estimate of measurement uncertainty that is currently not available from conventional geophone measurements. In what follows, we outline a simulation framework to test our method, our signal separation strategy, and test its effectiveness for a range of scenarios. We establish guidelines for when our method would be effective by measuring the signal-to-noise ratio (SNR) for various realistic combinations of sensor rotation angle, maximum peak seismic signal, and density of point measurements on the ground. We conclude by outlining technological advances needed to realize airborne seismic acquisition.

J. Unmanned Veh. Sys. Downloaded from cdnsciencepub.com by Thomas Rapstine on 12/16/21
For personal use only.

2. Methods

2.1. Airborne sensor motion model

Establishing an airborne sensor motion model is necessary to simulate how a sensor mounted on a drone moves. In our work, we denote time as t_i for $i \in \{0, \ldots, T-1\}$ where samples are separated by a constant interval Δt and T denotes the number of times. We refer the reader to Appendix A for a complete list of variables used in equations throughout our paper. We denote the position of the sensor as $\boldsymbol{r}_i = (r_x[i], r_y[i], r_z[i])^{\mathrm{T}}$ and the orientation as $\boldsymbol{\theta}_i = (\theta_x[i], \theta_y[i], \theta_z[i])^{\mathrm{T}}$ for $i \in \{0, ..., T-1\}$. $\boldsymbol{\theta}$ contains the Euler angles about the x-, y-, and z-axes, which are necessary to describe 3D orientation. For example, a linear motion model may be written as

$$\boldsymbol{r}_i = \boldsymbol{r}_{\mathrm{c}} t_i + \boldsymbol{r}_0 \tag{1}$$

$$\boldsymbol{\theta}_i = \boldsymbol{\theta}_{\mathrm{c}} t_i + \boldsymbol{\theta}_0 \tag{2}$$

where $\boldsymbol{r}_0 \in \mathbb{R}^{3\times1}$ is the initial position of the sensor, $\boldsymbol{\theta}_0 \in \mathbb{R}^{3\times1}$ its initial orientation, and $\boldsymbol{r}_{\mathrm{c}} \in \mathbb{R}^{3\times1}$ and $\boldsymbol{\theta}_{\mathrm{c}} \in \mathbb{R}^{3\times1}$ denote the rate of change in its position and orientation, respectively. In other words, $\boldsymbol{r}_{\mathrm{c}}$ and $\boldsymbol{\theta}_{\mathrm{c}}$ are the translation and rotation of the sensor from its original position and orientation at t_0. Other motion models could include higher order terms, such as t^2 or t^3, or even contain periodic terms involving trigonometric functions if sensor vibration is suspected. In reality, the appropriate sensor motion model depends on the sensor stabilization system. A high-quality stabilization system may eliminate sensor vibrations, but a lower quality and more realistic system may result in residual sensor vibration that would be necessary to account for in the sensor motion model. We keep the concept of the sensor motion model general and only assume it is a function of time; that way our separation strategy can be used for a variety of motion model situations.

Given a sensor's position and orientation, we construct a matrix that performs a coordinate system transformation from a (global) world coordinate system to the sensor's local coordinate system. We use the term global or world coordinate system to refer to the reference coordiante system in which the airborne sensor moves. In our examples, the initial position and orientation of the airborne sensor are chosen as the world coordinate system. We denote the rotation matrix for the sensor at t_i as $\mathbf{R}_i \in \mathbb{R}^{3\times3}$, which is formed using $\boldsymbol{\theta}_i$. There are multiple ways to describe a rotation matrix (Diebel 2006); one simple way is to construct $\mathbf{R}$ as

$$\mathbf{R} = \mathbf{R}_x \mathbf{R}_y \mathbf{R}_z \tag{3}$$

where

$$\mathbf{R}_x = \begin{pmatrix} 1 & 0 & 0 \\ 0 & \cos(\theta_x) & -\sin(\theta_x) \\ 0 & \sin(\theta_x) & \cos(\theta_x) \end{pmatrix} \tag{4}$$

$$\mathbf{R}_y = \begin{pmatrix} \cos(\theta_y) & 0 & \sin(\theta_y) \\ 0 & 1 & 0 \\ -\sin(\theta_y) & 0 & \cos(\theta_y) \end{pmatrix} \tag{5}$$

and

J. Unmanned Veh. Sys. Downloaded from cdnsciencepub.com by Thomas Rapstine on 12/16/21
For personal use only.

$$\mathbf{R}_z = \begin{pmatrix} \cos(\theta_z) & -\sin(\theta_z) & 0 \\ \sin(\theta_z) & \cos(\theta_z) & 0 \\ 0 & 0 & 1 \end{pmatrix} \tag{6}$$

Note that in eqs. (3)–(6) we have used $\mathbf{R}$ in place of $\mathbf{R}_i$ to simplify notation. We use $\mathbf{R}_i$ and the position of the sensor $\boldsymbol{r}_i$ to form a matrix $\mathbf{H}_i \in \mathbb{R}^{4\times4}$ that represents a coordinate transformation from a (global) world coordinate system to the (local) coordinate system of the airborne sensor at t_i

$$\mathbf{H}_i = \begin{pmatrix} \mathbf{R}_i & \boldsymbol{r}_i \\ \mathbf{0} & 1 \end{pmatrix} \tag{7}$$

Conversely, we can transform a point from the sensor's coordinate system into world coordinates using the inverse transformation

$$\mathbf{H}_i^{-1} = \begin{pmatrix} \mathbf{R}_i^{\mathrm{T}} & -\mathbf{R}_i^{\mathrm{T}}\boldsymbol{r}_i \\ \mathbf{0} & 1 \end{pmatrix} \tag{8}$$

To apply the coordinate transformation matrices $\mathbf{H}_i$ or $\mathbf{H}_i^{-1}$ to a 3D point, $\boldsymbol{x} = (x_1, x_2, x_3)^{\mathrm{T}}$, we must represent the position $\boldsymbol{x}$ in homogenous coordinates as

$$\widetilde{\boldsymbol{x}} = \begin{pmatrix} x_1 \\ x_2 \\ x_3 \\ 1 \end{pmatrix} \tag{9}$$

Homogeneous coordinates are commonly used in computer vision applications of projective geometry since they allow a coordinate system transformation to be represented using a single matrix–vector product (Szeliski 2011). Hereinafter we denote by a tilde $\widetilde{(\cdot)}$ the points or sets that are expressed in homogeneous coordinates. A point $\widetilde{\boldsymbol{x}}$ in homogenous coordinates can be represented in 3D coordinates by dividing by the fourth element in $\widetilde{\boldsymbol{x}}$:

$$\widetilde{\boldsymbol{x}} = \begin{pmatrix} a \\ b \\ c \\ d \end{pmatrix} \rightarrow \boldsymbol{x} = \begin{pmatrix} a/d \\ b/d \\ c/d \end{pmatrix} = \begin{pmatrix} x_1 \\ x_2 \\ x_3 \end{pmatrix} \tag{10}$$

$\mathbf{H}_i$ represents how points in the world coordinate system appear in the sensor's local coordinate system, which varies with time as does the seismic signal. A primary goal necessary for realizing airborne seismic acquisition is to remove the effects of $\mathbf{H}_i$ from sensor measurements of displacement to only recover ground displacement due to seismic wave propagation.

2.2. Defining a seismic signal model

We establish a seismic signal model with compact support in time that describes the translation of the ground surface observed by an airborne sensor mounted on a drone. The concept of compact support physically represents a seismic signal that is non-zero for a finite amount of time and is a convenient property that allows us to establish a tractable signal separation strategy. A seismic signal observed by a rotating and translating sensor would appear to be non-zero even if the seismic signal is zero. However, if we assume that

J. Unmanned Veh. Sys. Downloaded from cdnsciencepub.com by Thomas Rapstine on 12/16/21
For personal use only.

observation begins before the seismic signal is non-zero and ends after the support of the seismic signal, then we know that nonzero observations at the beginning and end of the measurement are only caused by the sensor motion. Thus, outside the support of the seismic signal, we can use displacement measurements to estimate the sensor motion model parameters (e.g., $\boldsymbol{r}_c$, $\boldsymbol{r}_0$, $\boldsymbol{\theta}_c$, or $\boldsymbol{\theta}_0$) without worrying about the effects of the seismic signal.

We choose to use discrete wavelets to reconstruct the seismic signal since, by design, discrete wavelets have compact support and can resemble seismic signals. We use Daubechies wavelets with two vanishing moments since they appear wave-like and are efficient to compute (Daubechies 1988). We denote the 3D seismic signal as $\mathbf{s}_i = (s_x[i], s_y[i], s_z[i])$ for $i \in \{0, \ldots, T-1\}$. Each component of $\mathbf{s}$ is independently constructed using a linear combination of N randomly shifted Daubechies wavelets at random scales; we only consider wavelets whose support is limited in $[a, b]$, where $a > 0$ and $b < T$. By only including wavelets with support in the interval $[a, b]$ we assume, physically, that the seismic signal is only non-zero in that particular interval. We label a random variable representing these wavelets as W, and note samples drawn from W as $w \in \mathbb{R}^{T\times 1}$. Using randomly generated w, we construct each component of $\mathbf{s}$ as

$$s_x = c\sum_{n=0}^{N-1} w \tag{11}$$

$$s_y = c\sum_{n=0}^{N-1} w \tag{12}$$

$$s_z = c\sum_{n=0}^{N-1} w \tag{13}$$

where $n = \{0, 1, \ldots, N-1\}$ and the weight c is chosen such that the maximum peak amplitude of $\mathbf{s}$ is $s_{\max}$. The resulting seismic signals look realistic and has the benefit of being randomly generated (Fig. 1). We use these randomly generated signals to construct synthetic seismic data for testing our signal separation method.

2.3. Topography as a randomly generated smooth surface

The simulated seismic signals translate the ground surface topography, which we represent as a set of k points sampling a surface of varying smoothness. We refer to this set as a point cloud, which can be represented as a matrix

$$\mathbf{P} = (\boldsymbol{p}_0 \quad \boldsymbol{p}_1 \quad \ldots \quad \boldsymbol{p}_{k-1}) \tag{14}$$

where each column of $\mathbf{P}$ contains the 3D coordinates of a point. Points in the columns of $\mathbf{P}$ lie on a $n_x \times n_y$ grid (where $k = n_x \times n_y$) where the spacing between points is Δx in the x-direction and Δy in the y-direction. The z-coordinate (i.e., topography) at each point is populated with values drawn from a uniform distribution between $z_{\min}$ and $z_{\max}$. This enables us to generate many random point clouds that lie on the same grid in x and y. Since the point cloud x and y coordinates lie on a grid, we can conceptualize it as a 2D function, or image, of topography (the z-coordinates in the point cloud). To induce a certain smoothness on the topography, we apply a 2D isotropic Gaussian filter characterized by a standard deviation of σ_t to the gridded z-coordinates. Near the edges of the grid we assume a zero-slope condition when applying the filter, ensuring consistently smooth topography near the edges. Large values of σ_t lead to point clouds that sample smoother surfaces; smaller values of σ_t lead to less smooth point clouds (Fig. 2).

J. Unmanned Veh. Sys. Downloaded from cdnsciencepub.com by Thomas Rapstine on 12/16/21
For personal use only.

Fig. 1. (*a* and *b*) Examples of randomly generated 3D seismic signals. The signals shown have compact support in the interval [0.2, 0.8] s. We estimate the sensors' motion model using measurements taken outside the seismic signal support, then infer it inside the seismic signal support using an assumed sensor motion model.

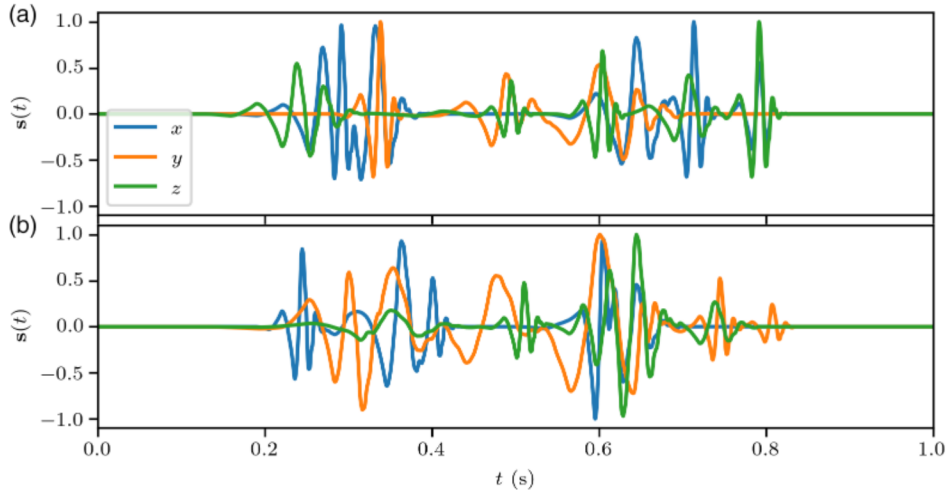

Fig. 2. Map-view of simulated topography with varying smoothness: (*a*) no smoothing, (*b*) smoothing with $\sigma_t = 1$, and (c) $\sigma_t = 2$. Topography is translated by a seismic signal during our simulations and has the benefit of being randomly generated.

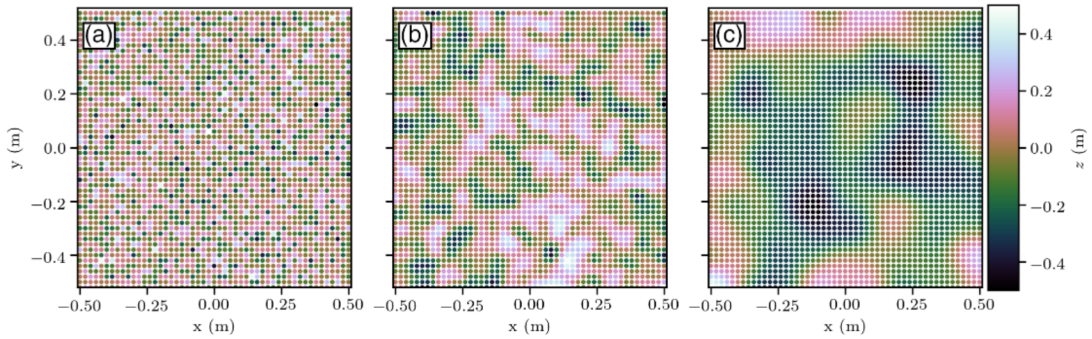

2.4. Simulating a moving surface as viewed from a noisy airborne sensor

We seek to represent the ground surface moved by a seismic wave as viewed from a noisy drone-mounted airborne sensor that repeatedly measures the position of points on the ground, and that is also moving and rotating. To do this, we represent a dynamic point cloud by first translating all points in $\mathbf{P}$ by $\mathbf{s}_i$. Then we apply a rigid-body transformation to all points using the coordinate transformation matrix $\mathbf{H}_i$ to represent them in the sensor's coordinate system at t_i. At each time t_i we observe a point cloud, represented as a matrix $\widetilde{\mathbf{Q}}_i \in \mathbb{R}^{4\times k}$, whose columns are

$$\widetilde{\mathbf{q}}_j = \mathbf{H}_i(\widetilde{\mathbf{p}}_j + \widetilde{\mathbf{s}}_i) \quad (15)$$

for $j \in \{0, \ldots, k-1\}$. We note that the columns of $\widetilde{\mathbf{Q}}_i$ are in homogenous coordinates, and can be represented in non-homogenous coordinates as the columns of an equivalent

matrix, $\mathbf{Q}_i \in \mathbb{R}^{3\times k}$. $\mathbf{Q}_i$ represents the position of all points on the ground at time t_i as observed from a noiseless sensor's coordinate system. Our objective is to undo each rigid-body transformation $\mathbf{H}_i$ to separate out the seismic signal $\mathbf{s}$. Moreover, we simulate noisy observations, $\hat{\mathbf{Q}}_i$, by adding noise drawn from a Gaussian distribution with zero mean and standard deviation σ to each observation in $\mathbf{Q}_i$. Uncorrelated noise is added independently to each point for each component (x, y, z) at each time t_i.

2.5. Separating sensor motion from seismic signals

We leverage an airborne sensor motion model (e.g., eq. (1)) and the assumed compact support of the seismic signal $\mathbf{s}$ to develop a tractable signal separation strategy. Our strategy is to use observations to find the position and orientation of the airborne sensor outside the support of the seismic signal, then use knowledge of the sensor motion model (eq. (1)) to infer the position and orientation of the airborne sensor during the support of the seismic signal. To describe this strategy, it is convenient to denote the indices $i_{\text{in}} = \{a, a+1, \ldots, b-1\}$ and $i_{\text{out}} = \{0, 1, \ldots, a-1, b, b+1, \ldots, T-1\}$ as those inside and outside the support of the seismic signal $\mathbf{s}$, respectively. The times corresponding to i_{in} and i_{out} are denoted as t_{in} and t_{out}, respectively.

Let us first consider how to find the motion of the airborne sensor outside the support of the seismic signal during t_{out}. At $t_0 = 0$ the seismic signal does not influence the observations of the topography, therefore we define the world coordinate system origin and orientation as the initial position and orientation of the airborne sensor. This implies that at t_0 the point cloud representing topography in world coordinates is equal to the point cloud represented in the airborne sensor's coordinates

$$\mathbf{Q}_0 = \mathbf{P} \tag{16}$$

In addition, this implies that the initial position and orientation of the airborne sensor are

$$\boldsymbol{r}_c = (0,0,0)^{\mathrm{T}} \tag{17}$$

and

$$\boldsymbol{\theta}_c = (0,0,0)^{\mathrm{T}} \tag{18}$$

respectively. As the sensor translates and rotates during t_{out} each point at the ground surface is observed as

$$\tilde{\mathbf{q}}_j = \mathbf{H}_i \tilde{\mathbf{p}}_j \tag{19}$$

or in physical coordinates as

$$\mathbf{q}_j = \mathbf{R}_i \mathbf{p}_j + \boldsymbol{r}_i \tag{20}$$

Considering all $\mathbf{q}_j$ at a single time $t_i \in t_{\text{out}}$ we form a matrix of observations as

$$\mathbf{Q}_i = \begin{pmatrix} \mathbf{R}_i \mathbf{p}_0 + \boldsymbol{r}_i & \ldots & \mathbf{R}_i \mathbf{p}_{k-1} + \boldsymbol{r}_i \end{pmatrix} \tag{21}$$

or equivalently

$$\mathbf{Q}_i = \mathbf{R}_i \mathbf{P} + \mathbf{T}_i \tag{22}$$

J. Unmanned Veh. Sys. Downloaded from cdnsciencepub.com by Thomas Rapstine on 12/16/21
For personal use only.

J. Unmanned Veh. Sys. Downloaded from cdnsciencepub.com by Thomas Rapstine on 12/16/21
For personal use only.

where $\mathbf{T}_i \in \mathbb{R}^{3\times k}$ has columns that are repeating representations of the airborne sensor translation at t_i

$$\mathbf{T}_i = (\,\boldsymbol{r}_i \quad \boldsymbol{r}_i \quad \ldots \quad \boldsymbol{r}_i\,) \tag{23}$$

Equation (22) shows that during t_{out} the observations $\mathbf{Q}_i$ are a rotated version of the point cloud $\mathbf{P}$ added to the translation of the airborne sensor. This also implies that $\mathbf{Q}_i$ is a rigid body transformed version of $\mathbf{P}$. We can solve for the rotation $\mathbf{R}_i$ and translation $\mathbf{T}_i$ in a least-squares sense using the strategy for finding rigid-body transformations between point clouds developed by Arun et al. (1987) (see Appendix B).

We utilize the sensor rotations and translations found during t_{out} to infer those during t_{in} such that they adhere to our airborne sensor motion model (e.g., eq. (1)). More complicated motion models are also possible and do not reduce the generality of our method. For example, if the sensor is not stabilized well and periodic sensor vibration is suspected, we may infer the dominant phase and frequency spectra of the sensor motion using Fourier analysis. Nonlinear non-periodic motion models may involve regressing the coefficients belonging to the first few polynomials that explain well the sensor's motion during t_{out}. Linear sensor translation would require us to infer translation during t_{in} by linear regression applied to all $(t_i, \boldsymbol{r}_i)$ for $t_i \in t_{\text{out}}$. If sensor orientations are linearly varying, we could use spherical linear interpolation on rotation matrices found during t_{out} (Shoemake 1985). We stress that if the assumed motion model does not explain well the measurements during t_{out}, then the motion model must be modified (perhaps by adding higher order terms or periodic terms) until it explains well the measurements. For example, if a linear translation motion model is assumed, yet a clear quadratic residual remains after fitting a line to measurements during t_{out}, then a quadratic term must be added to the motion model. Perhaps, a motion model may even be learned using the measurements obtained during t_{out} via a machine learning technique. After all $\mathbf{T}_i$ and $\mathbf{R}_i$ are found, we infer the seismic signal $\mathbf{s}$ by undoing rotations and translations during t_{in}. During $t_i \in t_{\text{in}}$ the observations $\mathbf{Q}_i$ are rigid-body transformations of the topography perturbed by $\mathbf{s}$. Specifically, during $t_i \in t_{\text{in}}$ each point in a point cloud observed by the moving sensor is described by

$$\widetilde{\mathbf{q}}_j = \mathbf{H}_i(\widetilde{\mathbf{p}}_j + \widetilde{\mathbf{s}}_i) \tag{24}$$

or

$$\mathbf{q}_j = \mathbf{R}_i(\mathbf{p}_j + \mathbf{s}_i) + \boldsymbol{r}_i \tag{25}$$

Considering all $\mathbf{q}_j$ at a single time $t_i \in t_{\text{in}}$ we form a matrix of observations as

$$\mathbf{Q}_i = \mathbf{R}_i(\mathbf{P} + \mathbf{S}_i) + \mathbf{T}_i \tag{26}$$

where $\mathbf{S}_i \in \mathbb{R}^{3\times k}$ has columns that are repeating representations of the seismic signal translation at t_i

$$\mathbf{S}_i = (\,\mathbf{s}_i \quad \mathbf{s}_i \quad \ldots \quad \mathbf{s}_i\,) \tag{27}$$

The solution for the separated seismic signal at t_i is then

$$\mathbf{S}_i = \mathbf{R}_i^{\mathrm{T}}(\mathbf{Q}_i - \mathbf{T}_i) - \mathbf{P} \tag{28}$$

Here we use the transpose of the rotation matrix $\mathbf{R}_i^{\mathrm{T}}$ as its inverse, since rotation matrices are orthogonal.

J. Unmanned Veh. Sys. Downloaded from cdnsciencepub.com by Thomas Rapstine on 12/16/21
For personal use only.

We can also obtain an estimate of uncertainty for the separated seismic signal by collectively considering the columns $\mathbf{S}_i$, noted as $\hat{\mathbf{S}}_i$, derived from noisy measurements at a particular time t_i. The columns of $\hat{\mathbf{Q}}_i$, and therefore $\hat{\mathbf{S}}_i$, correspond to points on the ground surface. Assuming that the noise in $\hat{\mathbf{Q}}_i$ is independent of the point being observed, and that all points undergo the same translation, we can collectively consider estimates of displacements for all points to obtain an estimate of uncertainty. Specifically, we can consider each column of $\mathbf{S}_i$ as an estimate of the seismic signal at t_i; the collection of all columns of $\hat{\mathbf{S}}_i$ can be considered as many noise observations of displacement. We take the estimate and uncertainty of the seismic signal at time t_i to be the mean and standard deviation, respectively, of the columns of $\hat{\mathbf{S}}_i$.

In summary, our method for separating sensor motion from seismic signals is as follows:

1. Repeatedly measure the position of many points $\mathbf{P}$ on the ground surface using an airborne sensor that is moving before, during, and after a seismic signal displaces the ground.
2. Reconstruct the sensor motion outside the support of the seismic signal $\mathbf{Q}_i$ for $i \in i_{\text{out}}$ using rigid-body transformation between point clouds measured at consecutive times (e.g., at t_i and t_{i+1} for $i \in i_{\text{out}}$) (see Appendix B).
3. Reconstruct the sensor motion inside the support of the seismic signal $\mathbf{Q}_i$ for $i \in i_{\text{in}}$ using a sensor motion model assumption (e.g., smoothness, linearity, periodicity, sparsity, etc.).
4. Reconstruct the displacement of each point at the ground surface $\hat{\mathbf{S}}$ using the reconstructed sensor motion (eq. (28)).
5. Estimate the seismic signal $\hat{\mathbf{s}}$ as the mean of the columns of $\hat{\mathbf{S}}$ and establish the uncertainty of the seismic signal as the standard deviation of the columns of $\hat{\mathbf{S}}$.

3. Results and discussion

We divide our results into a series of experiments that illustrate the scenarios under which we can use our signal separation strategy to measure seismic signals from an airborne sensor in practice. We identify parameters that exhibit successful seismic signal estimates by measuring the SNR; we use the convention that SNR > 0 dB indicates success while a SNR < 0 dB indicates failure. We use the definition for SNR in dB that follows:

$$\text{SNR} = 10\log_{10}\left(\frac{\|s_i\|^2}{\|s_i - \hat{s}_i\|^2}\right) \tag{29}$$

where s_i is one component of the true seismic signal and $\hat{s}_i$ is the corresponding estimate of s_i we estimate from our measurements (i.e., the mean of the ith row of the matrix $\hat{\mathbf{S}}$). In each experiment, we construct topography over a 1 m^2 area using a rugosity corresponding to $\sigma_t = 25$ cm, equal sample spacing $\Delta x = \Delta y = 1$ cm, and $N = 7$ wavelets. In all experiments, we simulate an airborne sensor at a height of 2 m above the ground with linear sensor rotation and translation equally applied about and along the x-, y-, and z-axes. We use a time sampling interval of 1 ms in our simulations, which is comparable to the sampling rate of a typical geophone used in seismic exploration. In each experiment, we recover a seismic signal that is 1 s long with compact support in $t \in [0.2, 0.8]$ s. This duration (0.6 s) for a seismic signal is on the order of a typical seismic shot record; however, our method works on each time t_i independently, and thus, generalizes to longer seismic signals.

3.1. Seismic signal separation in noiseless observations

We first verify that our methodology recovers a seismic signal when no noise is present. To do so, we set the sensor height at 2 m above the ground, induce linear sensor translation of 10 cm about all axes, induce linear sensor rotation of 1° about all axes, and generate seismic signals with a maximum seismic signal peak of $s_{\max} = 1$ mm to simulate

Fig. 3. (*a*) Noiseless observation, (*b*) true seismic signal, and (*c*) estimated seismic signal. Note that the (*a*) noiseless observations are several orders of magnitude greater than the (*b*, *c*) seismic signal. The subtle curvature in (*a*) noiseless observations is due to sensor rotation.

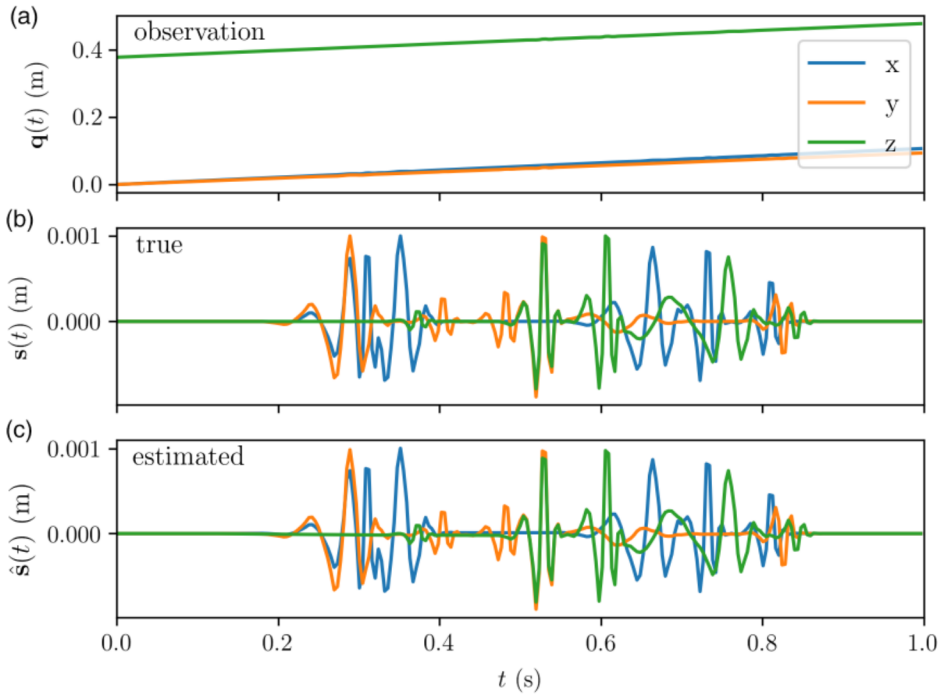

observations $\mathbf{Q}_i$ for $i \in \{0, 1, \ldots, T-1\}$. The rotation we simulate is small, but a translation of 10 cm is a considerable distance for a stabilized sensor to move over the course of 1 s. We assume an airborne sensor motion model that is linear in translation and rotation. The resulting observations are slightly curved due to the linear rotation over time and are orders of magnitude larger than the seismic signal (Fig. 3*a*). The seismic signal recovered using our signal separation strategy shows excellent signal recovery for each of the three signal components and is nearly indistinguishable from the true signal (Figs. 3*b* and 3*c*). This shows that our signal separation strategy works with zero observational noise for small $s_{\max}$, small sensor rotations of 1°, and modest sensor translations of several centimetres. Next, we explore the reality of recovering a seismic signal from noisy observations.

3.2. Seismic signal separation in noisy observations

We develop an understanding of how our methodology behaves as the observational noise (σ) increases by repeating the experiment described earlier with varying levels of noise and identifying when SNR drops below 0. We consider noise between $\sigma = 0$ mm and 10 cm; a generous range of noise values for modern laser- or camera-based sensors measuring distances roughly 2 m away (the initial height of our sensor above the ground). The recovered 3D seismic signal for two noise levels $\sigma = 0.5$ and 1.0 mm shows that, unsurprisingly, our uncertainty increases as the noise in our measurements increases (Fig. 4). We analyze how noise affects our separation more completely by conducting 31 simulations for each noise level between $\sigma = 1$ mm and 10 cm and plotting the resulting

J. Unmanned Veh. Sys. Downloaded from cdnsciencepub.com by Thomas Rapstine on 12/16/21
For personal use only.

J. Unmanned Veh. Sys. Downloaded from cdnsciencepub.com by Thomas Rapstine on 12/16/21
For personal use only.

Fig. 4. (*a*) True seismic signal and (*b* and *f*) simulated noisy observations for (*c*–*e*) $\sigma = 0.5$ mm and (*g*–*i*) $\sigma = 1.0$ mm. Solid colors in (*c*–*e*) and (*g*–*i*) show each component of the mean recovered 3D seismic signal; shaded regions show the standard deviation of the estimated signal. (*c*–*e*) Recovery with a noise level $\sigma = 0.5$ mm shows lower uncertainty than that recovered using (*g*–*i*) a higher noise level $\sigma = 1.0$ mm.

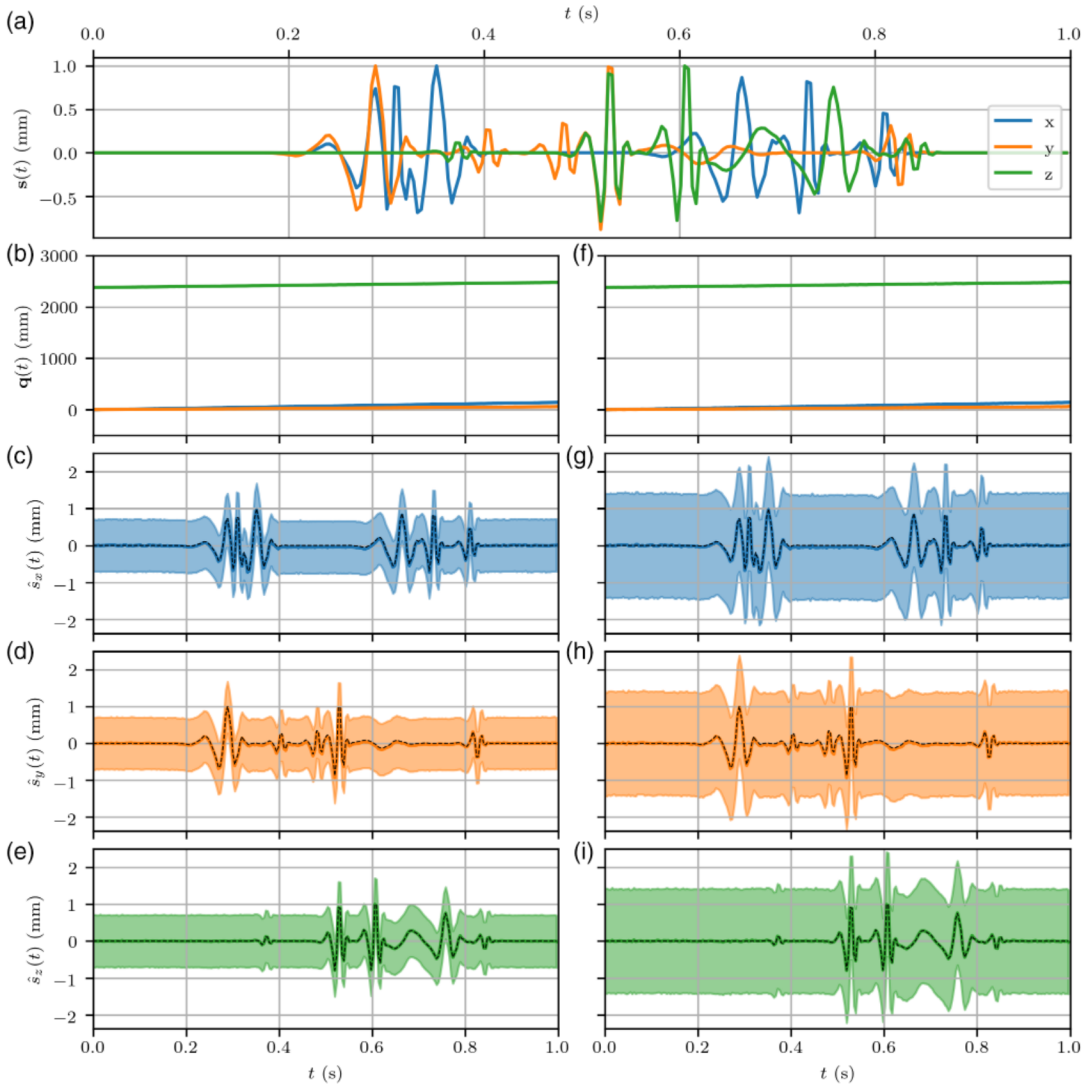

SNR (Fig. 5). As expected, for all components of **s**, the SNR decreases as we add noise to our observations; SNR for the *x*-, *y*-, and *z*-component drops below 0 at $\sigma = 15$ mm (see Fig. 5). However, SNR for the *z*-component is consistently higher than the *x*- or *y*-components' SNR for lower noise levels ($\sigma < 1$ mm) (Fig. 5). The lower SNR for the *x*- and *y*-components is expected since our topography is mostly planar (extending in the *x*- and *y*-directions); the *x*- and *y*-components of each point observed by the sensor are the most affected by sensor rotation, whereas the *z*-component is less affected. This encouraging result implies that an airborne sensor can have a noise level that is roughly 15 times as high as the peak signal in **s** and still achieve a SNR > 0 from a sensor height of 2 m.

Fig. 5. Derived SNR as a function of observational noise σ. We observe that SNR for x- and y- components are consistently lower than the z- component SNR for noise levels below $\sigma = 1$ mm due to topography being mostly planar. We also observe that SNR > 0 for $\sigma < 15$ mm for all components.

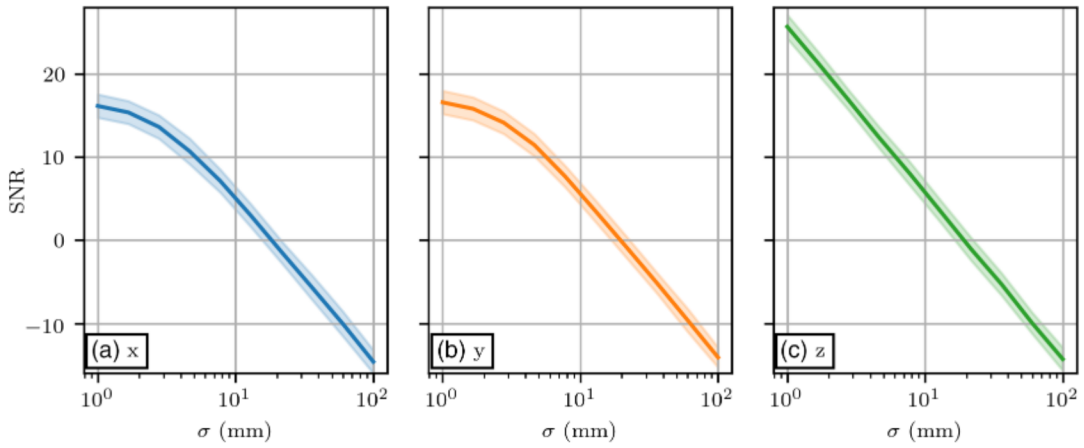

Fig. 6. Derived SNR as a function of sensor rotation θ. We observe smaller SNR for x- and y-components compared to the z-component due to topography being mostly planar; rotation affects the x- and y-components of the points on the ground more than the z-component.

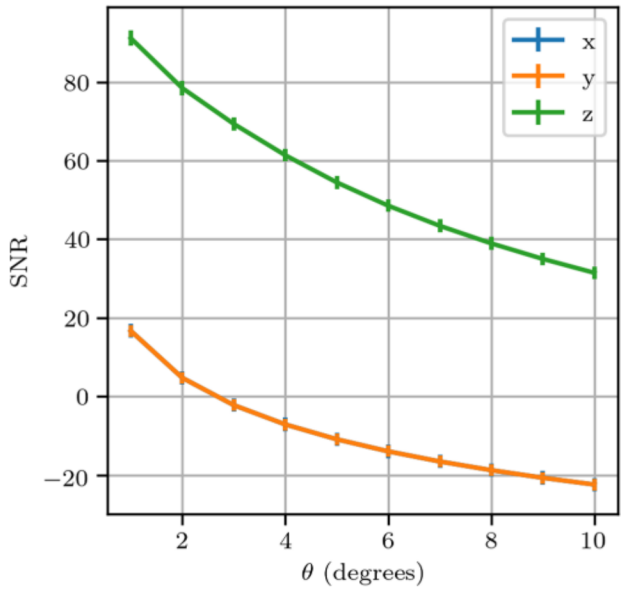

3.3. Separation dependency on sensor rotation

We continue our analysis of how well signal separation performs by considering SNR as a function of sensor rotation angle. We repeat the noiseless experiment in Sect. 3.1 for a range of sensor rotation angles between 0° and 10°, which is a reasonable range of angles relevant to stabilized sensors. Results show, again, that the x- and y-components have consistently lower SNR than the z-component (Fig. 6). We observe that SNR < 0 below about $\theta = 2.75°$ for the x- and y-components, but that SNR > 0 for angles up to and beyond

J. Unmanned Veh. Sys. Downloaded from cdnsciencepub.com by Thomas Rapstine on 12/16/21
For personal use only.

J. Unmanned Veh. Sys. Downloaded from cdnsciencepub.com by Thomas Rapstine on 12/16/21
For personal use only.

Fig. 7. Signal-to-noise ratios for (*a*) *x*-, (*b*) *y*-, and (*c*) *z*-components of estimated seismic signal as a function of observation noise and peak signal amplitude. When the peak signal amplitude is close to the noise level we are able to recover the signal. Blue areas of each subplot denote SNR < 0 and indicate failure; red areas denote SNR > 0 and indicate success. We denote the failure boundary for each component using a solid black line in each subplot to indicate SNR = 0. Below the failure boundary our method succeeds to recover seismic signals.

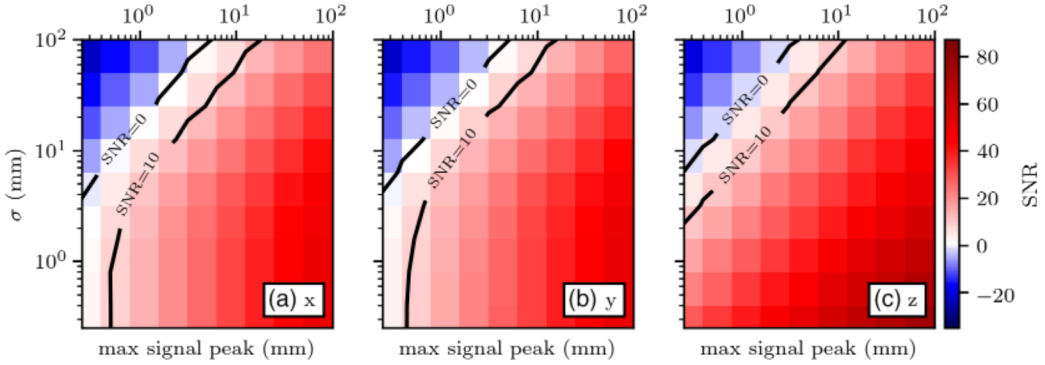

$\theta = 10.0°$. The *z*-component SNR > 1 for all angles below 10°. Thus, the recovery of the *x*-component is more robust to sensor rotation angle changes than the *x*- and *y*- components.

3.4. Separation dependency on sensor noise level and max peak signal

Our signal separation strategy is affected by both the sensor noise level (σ) and maximum signal peak (s_{max}), thus, we jointly analyze how separation performs for many combinations of σ and s_{max}. We seek to identify a boundary in (σ, s_{max})-space that defines when our separation fails (i.e., when SNR = 0). We find this boundary by measuring SNR for recovered signals resulting from simulations with the sensor height at 2 m, $\sigma \in [0.1\,\text{mm}, 1\,\text{cm}]$, and $s_{max} \in [0.1\,\text{mm}, 1\,\text{cm}]$. The resulting SNR maps for each component (Fig. 7) show combinations of (σ, s_{max}) that result in SNR > 0. We define the SNR = 0 failure boundary (solid black line in Fig. 7) in each SNR map to highlight combinations of (σ, s_{max}) that result in successfully separated seismic signals; areas in red in Fig. 7 show viable (σ, θ) combinations, whereas blue areas highlight combinations that result in an unsuccessful signal separation.

In the *x*- and *y*-component SNR maps (Figs. 7*a*–*b*) we observe that SNR does not change as a function of σ when s_{max} is below about 0.5 mm. We interpret this as a consequence of the sample spacing (in this particular case $\Delta x = \Delta y = 1$ cm) of our point clouds being large compared to s_{max} and σ. We cannot recover the *x*- and *y*-component of signals that are both far below the noise level and also far below our sampling in Δx and Δy. This feature is not observed in the *z*-component SNR map (Fig. 7) since our topography is mostly planar; the *z*-coordinates are all very similar and represent a finer sample density along *z* compared to the sampling in *x* and *y*. Regardless, we find that that the failure boundary is approximately linear, and has a slope of approximately 20 for all components of displacement. Thus, from a 2 m height we can achieve SNR > 0 with an airborne sensor with σ 20× greater than s_{max} (provided σ is below the failure boundary in Fig. 7). However, this conclusion relies on a sample spacing of $\Delta x = \Delta y = 1$ cm, which may vary based on the sensor of choice, thus we next explore variations in the failure boundary for various sample spacings.

J. Unmanned Veh. Sys. Downloaded from cdnsciencepub.com by Thomas Rapstine on 12/16/21
For personal use only.

Fig. 8. *SNR* maps for the *x*-, *y*-, and *z*- components of the estimated seismic signal as a function of σ and max signal peak for various $\Delta x = \Delta y =$ (*a*–*c*) 20 cm, (*d*–*f*) 10 cm, (*h*–*j*) 5 cm, and (*k*–*m*) 2.5 cm. We observe a general linear trend in the failure boundary at SNR = 0 marked as a black line on each subplot. These results imply that denser sample spacing results in higher SNR. We observe an exception of for SNR values below $\sigma = 5.0$ cm where we see a nonlinear trend develop indicating no improvement in SNR with a decrease in σ.

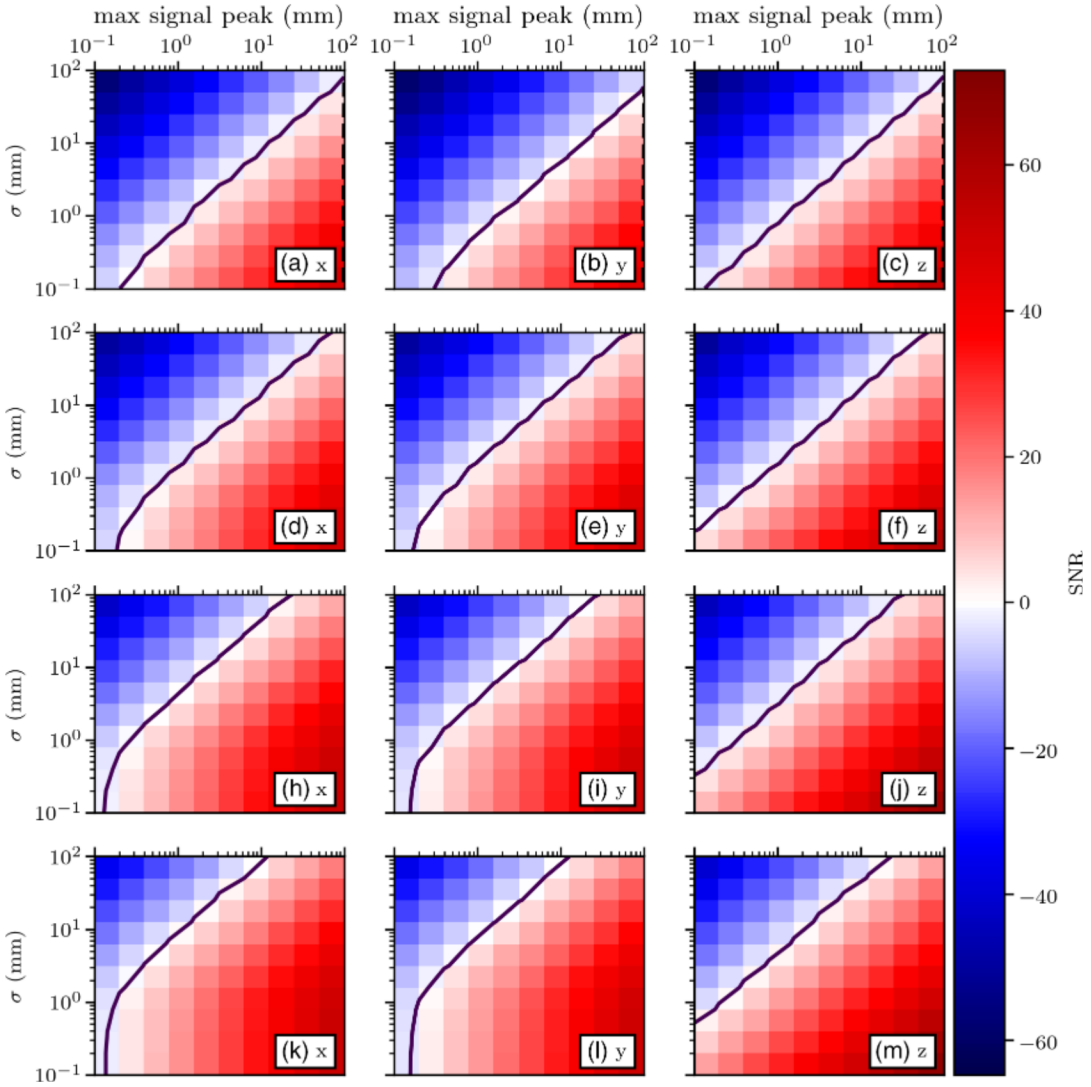

3.5. Separation dependency on sample spacing

The SNR achieved using our signal separation method improves as the sample spacing (Δx and Δy) decreases. We reach this conclusion by repeating the experiment in Sect. 3.4 where we measure SNR as a function of noise level (σ) and max peak signal ($s_{\max}$) for various values of point sample spacings on the ground $\Delta x = \Delta y \in \{20\,\text{cm}, 10\,\text{cm}, 5\,\text{cm}, 2.5\,\text{cm}\}$ within the same 1 m^2 area (see Fig. 8). In each SNR map for the different values of $\Delta x = \Delta y$ (Fig. 8) we find that the failure boundary, defined by SNR = 0, is approximately linear over most ranges of σ and θ for all options of $\Delta x = \Delta y$ (Fig. 9). A steeper failure boundary slope implies that, for a given value of σ along the failure boundary, we can measure signals with

J. Unmanned Veh. Sys. Downloaded from cdnsciencepub.com by Thomas Rapstine on 12/16/21
For personal use only.

Fig. 9. Failure boundaries defining SNR = 0 for (*a*) *x*-, (*b*) *y*-, and (*c*) *z*-components for varying sample spacings ($\Delta x = \Delta y$). Note that the failure boundaries here are plotted on a linear scale to highlight the differences in the slope of the failure boundary. The slope of each line is noted in Table 1. We find that smaller sample spacings give steeper failure boundaries. This indicates that for a given noise level on the failure boundary we can observe signals with smaller max signal peaks if we make measurements with denser sample spacings. The failure boundary slope roughly doubles if we halve the sample spacing.

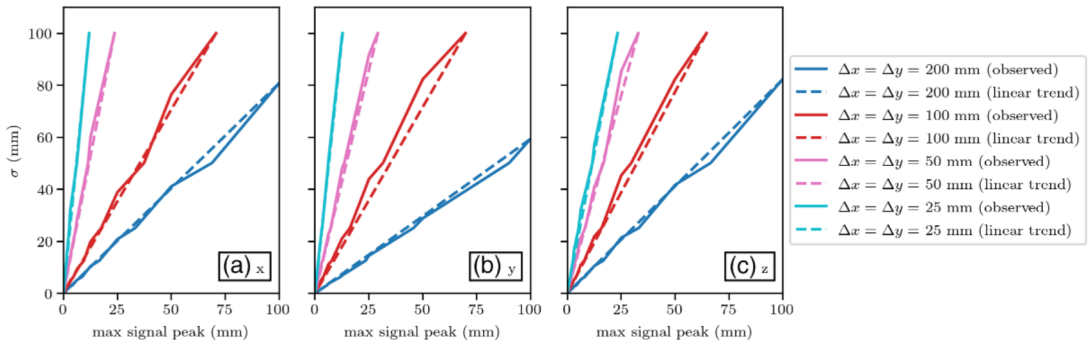

Table 1. Failure boundary slope for each component of the estimated seismic signal for various sample spacings ($\Delta x = \Delta y$).

	Slope of SNR failure boundary		
$\Delta x = \Delta y$	*x*	*y*	*z*
20 cm	0.808	0.594	0.823
10 cm	1.414	1.432	1.547
5 cm	4.225	3.436	3.033
2.5 cm	8.414	7.842	4.269

Note: The slope of the failure boundary quantifies the relationship between s_{max} and σ along the failure boundary. Higher slopes indicate that a higher sensor noise level σ can still achieve a given s_{max}.

smaller s_{max} if we increase the sample spacing of our measurements. We can more easily distinguish differences in the slope of each failure boundary by plotting them on a linear scale (Fig. 9). The slopes for each failure boundary are summarized in Table 1, where we see that the slope roughly doubles as we halve the sample spacing. This behavior implies that measuring denser points on the ground from an airborne sensor would substantially improve the SNR of recovered seismic signals.

4. Conclusion

In response to advances in drone and sensor technology, we develop a method for estimating and removing sensor rotation and translation from consecutive measurements of point coordinates on the ground for measuring a 3D seismic signal. Our method assumes that the seismic signal has a finite duration and that a sensor motion model is either known apriori or may be estimated from measurements made outside the support of the seismic signal. We achieve higher SNR when measurement noise level and sensor rotation angles are small, when the seismic signal amplitude is large, and when the sampling point density of the sensor is high. We define a failure boundary that helps identify what combinations of noise level and max peak signal allow for seismic signal recovery. Using the boundary, we conclude that a sensor with $\sigma \approx 1$ mm mounted on a drone at 2 m height is capable of measuring seismic signals with max peak signals above $s_{max} \approx 0.1$ mm provided that ground

sampling density is $\Delta x = \Delta y \leq 1$ cm, the sensor rotation $\theta \approx 1°$, and sensor translation is less than 10 cm. We find that increasing sampling point density can make achieving SNR > 0 more feasible. Our method for defining the failure boundary can be used to explore other sensor and ground motion combinations, and facilitates exploring the effects of correlated observational noise as well as more complex sensor motion models.

Acknowledgements

We thank the sponsor companies of the Center for Wave Phenomena, whose support made this research possible.

References

Arun, K.S., Huang, T.S., and Blostein, S.D. 1987. Least-squares fitting of two 3-D point sets. IEEE Trans. Pattern Anal. Mach. Intell. **9**(5): 698–700. doi:10.1109/TPAMI.1987.4767965.

Berni, A.J. 1991. Remote seismic sensing. U.S. Patent No. 5070483. [Issued 12 January 1990].

Berni, A.J. 1994. Remote sensing of seismic vibrations by laser Doppler interferometry. Geophysics, **59**(12): 1856–1867. doi:10.1190/1.1443573.

Center for Engineering Strong Motion Data. 2016. USGS Station OK034. Available from www.strongmotioncenter.org.

Chen, J.G., Wadhwa, N., Cha, Y.-J., Durand, F., Freeman, W.T., and Buyukozturk, O. 2014. Structural modal identification through high speed camera video: Motion magnification. Topics Mod. Anal. I, **7**: 191–197.

Courville, S., and Sava, P. 2019. Speckle noise in orbital laser doppler vibrometry. *In* Lunar and Planetary Science Conference, Vol. 50.

Courville, S.W. 2019. Toward orbital seismology: theory for speckle noise reduction in laser doppler vibrometer measurements on distant rough surfaces, Ph.D. thesis, Colorado School of Mines. Available from http://mines.idm.oclc.org/login?url=https://search.proquest.com/docview/2352101098?accountid=25386.

Daubechies, I. 1988. Orthonormal bases of compactly supported wavelets. Commun. Pure Appl. Math. **41**(7): 909–996. doi:10.1002/cpa.3160410705.

Davis, A., Rubinstein, M., Wadhwa, N., Mysore, G.J., Durand, F., and Freeman, W.T. 2014. The visual microphone: passive recovery of sound from video. ACM Transaction on Graphics, **33** (4): 1–10. doi:10.1145/2601097.2601119.

Diebel, J. 2006. Representing attitude: Euler angles, unit quaternions, and rotation vectors. Matrix, **58**(15–16): 1–35.

Dräbenstedt, A. 2014. Diversity combining in laser Doppler vibrometry for improved signal reliability. AIP Conf. Proc. **1600**: 263–273.

Dräbenstedt, A., Cao, X., Polom, U., Pätzold, F., Zeller, T., Hecker, P., et al. 2016. Mobile seismic exploration. AIP Conf. Proc. **1740**: 030001.

Longoni, L., Papini, M., Brambilla, D., Barazzetti, L., Roncoroni, F., Scaioni, M., and Ivanov, V.I. 2016. Monitoring riverbank erosion in mountain catchments using terrestrial laser scanning. Remote Sens. **8**(3): 241. doi:10.3390/rs8030241.

Neugirg, F., Stark, M., Kaiser, A., Vlacilova, M., Della Seta, M., Vergari, F., et al. 2016. Erosion processes in Calanchi in the Upper Orcia Valley, Southern Tuscany, Italy based on multitemporal high-resolution terrestrial LiDAR and UAV surveys. Geomorphology, **269**: 8–22. doi:10.1016/j.geomorph.2016.06.027.

O'Neal, M.A., and Pizzuto, J.E. 2011. The rates and spatial patterns of annual riverbank erosion revealed through terrestrial laser-scanner surveys of the South River, Virginia, Earth Surf. Process. Landf. **36**(5): 695–701.

Rabatel, A., Deline, P., Jaillet, S., and Ravanel, L. 2008. Rock falls in high-alpine rock walls quantified by terrestrial lidar measurements: A case study in the Mont Blanc area, Geophys. Res. Lett. **35**(10). doi:10.1029/2008GL033424.

Rapstine, T., and Sava, P. 2017. Measuring seismic signals with airborne stereo cameras. SEG Technical Program Expanded Abstracts 2017, Society of Exploration Geophysicists, pp. 5943–5947.

Rapstine, T., Sava, P., and Arias, E. 2017. Airborne seismic data acquisition using stereo vision. J. Unman. Vehicle Sys. **6**(1): 31–42.

Rembe, C., and Dräbenstedt, A. 2015. Speckle-insensitive laser-doppler vibrometry with adaptive optics and signal diversity. Proc. Sens. **2015**: 505–510.

Rengers, F.K., Rapstine, T.D., Olsen, M., Allstadt, K.E., Bunn, M., Iverson, R.M., et al. 2020. Using high sample rate lidar to capture debris-flow velocity and surface geometry. Environ. Eng. Geosci. **27**(1): 113–126.

Rengers, F.K., and Tucker, G.E. 2015. The evolution of gully headcut morphology: a case study using terrestrial laser scanning and hydrological monitoring. Earth Surf. Process. Landf. **40**(10): 1304–1317. doi:10.1002/esp.3721.

Rengers, F., Rapstine, T., Allstadt, K., Olsen, M., Bunn, M., Iverson, R., et al. 2019. Real-time monitoring of debris-flow velocity and mass deformation from field experiments with high sample rate lidar and video. *In* Proceedings of the Seventh International Conference on Debris-Flow Hazards Mitigation, Boulder, Colo., 10–13 June 2019. doi:10.25676/11124/173219.

Rubinstein, M. 2014. Analysis and visualization of temporal variations in video. Ph.D. thesis, Massachusetts Institute of Technology.

Shariati, A., Schumacher, T., and Ramanna, N. 2015. Eulerian-based virtual visual sensors to detect natural frequencies of structures. J. Civ. Struct. Health Monit. **5**: 457–468

Shahadi, H.I., Albattat, H.J., Al-allaq, Z.J., and Thahab, A.T. 2020. Eulerian video magnification: a review. Indones. J. Electr. Eng. Comput. Sci. **18**(2): 799–811. doi:10.11591/ijeecs.v18.i2.pp799-811.

J. Unmanned Veh. Sys. Downloaded from cdnsciencepub.com by Thomas Rapstine on 12/16/21
For personal use only.

Shearer, S.E. 2005. Three-dimensional inversion of magnetic data in the presence of remanent magnetization. Ph.D. thesis, Colorado School of Mines.
Shoemake, K. 1985. Animating rotation with quaternion curves. *In* Proceedings of the 12th Annual Conference on Computer Graphics and Interactive Techniques, San Francisco, Calif., 22–26 July 1985. pp. 245–254.
Szeliski, R. 2011. Computer vision: algorithms and applications. Springer. Available from http://www.visionbib.com/bibliography/book28.html#TT2007.
Wadhwa, N., Rubinstein, M., Durand, F., and Freeman, W.T. 2014. Riesz pyramids for fast phase-based video magnification. Computational Photography (ICCP), 2014 IEEE International Conference, Santa Clara, Calif., 2–4 May 2014. IEEE.
Wahbeh, A.M., Caffrey, J.P., and Masri, S.F. 2003. A vision-based approach for the direct measurement of displacements in vibrating systems. Smart Mater. Struct. **12**(5): 785. doi:10.1088/0964-1726/12/5/016.
Williams, J.G., Rosser, N.J., Hardy, R.J., Brain, M.J., and Afana, A.A. 2018. Optimising 4-D surface change detection: an approach for capturing rockfall magnitude–frequency. Earth Surf. Dyn. **6**(1): 101–119. doi:10.5194/esurf-6-101-2018.
Williams, J.G., Rosser, N.J., Hardy, R.J., and Brain, M.J. 2019. The importance of monitoring interval for rockfall magnitude-frequency estimation. J. Geophys. Res. Earth Surf. **124**(12): 2841–2853.
Wu, H.-Y., Rubinstein, M., Shih, E., Guttag, J.V., Durand, F., and Freeman, W.T. 2012. Eulerian video magnification for revealing subtle changes in the world. ACM Trans. Graph. **31**(4): 1. doi:10.1145/2185520.2185561.
Wu, H.-Y., Rubinstein, M., Shih, E.I., Guttag, J.V., Durand, F., Freeman, W.T., and Wadhwa, N. 2019. Linear-based eulerian motion modulation. US Patent, **10**: 217–218.

Appendix A. List of symbols

Table A1. Symbols representing time.

T	number of time steps
i	index of a variable in time
t_i	time at index i
i_{in}	set of indices inside the support of the seismic signal
i_{out}	set of indices outside the support of the seismic signal
t_{in}	set of times inside the support of the seismic signal
t_{out}	set of times outside the support of the seismic signal

Table A2. Symbols representing position and orientation of the airborne sensor.

r_x	x-position of the airborne sensor
r_y	y-position of the airborne sensor
r_z	z-position of the airborne sensor
$\boldsymbol{r}_i$	vector containing the x-, y-, and z-coordinates of the airborne sensor at time i
θ_x	Euler angle about the x-axis for the orientation of the airborne sensor
θ_y	Euler angle about the y-axis for the orientation of the airborne sensor
θ_z	Euler angle about the z-axis for the orientation of the airborne sensor
$\boldsymbol{\theta}_i$	vector containing Euler angles about x-, y-, and z-axis at time i
$\boldsymbol{r}_0$	initial position of the airborne sensor
$\boldsymbol{\theta}_0$	initial orientation of the airborne sensor
$\boldsymbol{r}_c$	rate of change in the position of the airborne sensor prescribed by our linear motion model
$\boldsymbol{\theta}_c$	rate of change in the orientation of the airborne sensor prescribed by our linear motion model
$\mathbf{R}_i$	rotation matrix at time i
$\mathbf{R}_x$	rotation matrix about the x-axis
$\mathbf{R}_y$	rotation matrix about the y-axis
$\mathbf{R}_z$	rotation matrix about the z-axis
$\mathbf{H}_i$	matrix that transforms point coordinates from global to local
$\tilde{\cdot}$	denotes that a variable is in homogeneous coordinates

J. Unmanned Veh. Sys. Downloaded from cdnsciencepub.com by Thomas Rapstine on 12/16/21
For personal use only.

Table A3. Symbols representing the sampling of the ground topography.

k	number of points sampled at the ground surface
j	index of a point sampled at the ground surface
n_x	width (in samples) of point grid in x-direction
n_y	width (in samples) of point grid in y-direction
Δx	spacing between samples at the ground surface in x
Δy	spacing between samples at the ground surface in y
$z_{\min}$	minimum z-coordinate of points sampled at the ground surface
$z_{\max}$	maximum z-coordinate of points sampled at the ground surface
σ_t	standard deviation of 2D isotropic Gaussian filter used to construct topography
σ	standard deviation of the Gaussian distribution used to add noise to observations
$\mathbf{P}_j$	a vector containing the position of point j on the ground surface
$\mathbf{P}$	a matrix containing a collection of all points on the ground surface in the global/reference coordinate system
$\mathbf{q}_j$	the position of point j as observed by the airborne sensor
$\mathbf{Q}_i$	a matrix containing a collection of point coordiantes as viewed from the sensor at time i

Appendix B. Estimating a rigid-body transformation between point clouds

A least-squares solution to the rigid-body transformation between two point clouds has previously been established by Arun et al. (1987). We briefly review this solution here. Consider matrices $\mathbf{A}, \mathbf{B} \in \mathbb{R}^{3\times k}$ whose corresponding columns represent k points in two point clouds. If $\mathbf{B}$ is $\mathbf{A}$ after rigid-body transformation then we may express $\mathbf{B}$ as

$$\mathbf{B} = \mathbf{R}\mathbf{A} + \mathbf{T} \tag{B1}$$

where $\mathbf{R} \in \mathbb{R}^{3\times 3}$ is a rotation matrix from $\mathbf{A}$ to $\mathbf{B}$, and $\mathbf{T} \in \mathbb{R}^{3\times k}$ contains the translation component of the rigid-body transformation in matrix form

$$\mathbf{T} = (\mathbf{t} \quad \dots \quad \mathbf{t}) \tag{B2}$$

where $\mathbf{t}$ is the translation from $\mathbf{A}$ to $\mathbf{B}$. Given observations of points in $\mathbf{A}$ and $\mathbf{B}$ we can find the least squares solution for $\mathbf{R}$ and $\mathbf{T}$ by minimizing

$$\text{err} = \sum_{i=0}^{k-1} \|\mathbf{R}\boldsymbol{a}_i + \mathbf{t} - \boldsymbol{b}_i\|^2 \tag{B3}$$

where $\boldsymbol{a}_i, \boldsymbol{b}_i \in \mathbb{R}^{3\times 1}$ denote corresponding points in each point set in corresponding columns of $\mathbf{A}$ and $\mathbf{B}$, respectively. The solution requires us to center each point cloud then deduce an optimal rotation between them by singular value decomposition. To center, we first compute the centroid of each x-, y-, and z-component of both $\mathbf{A}$ and $\mathbf{B}$ by

$$\boldsymbol{\mu}_A = \frac{1}{k}\sum_i^k \boldsymbol{a}_i \tag{B4}$$

and

$$\boldsymbol{\mu}_B = \frac{1}{k}\sum_i^k \boldsymbol{b}_i \tag{B5}$$

We then form the matrices for centering $\mathbf{A}$ and $\mathbf{B}$ as

$$\mathbf{M}_A = (\boldsymbol{\mu}_A \quad \boldsymbol{\mu}_A \quad \dots \quad \boldsymbol{\mu}_A) \tag{B6}$$

J. Unmanned Veh. Sys. Downloaded from cdnsciencepub.com by Thomas Rapstine on 12/16/21
For personal use only.

and

(B7) $$\mathbf{M}_B = (\boldsymbol{\mu}_B \quad \boldsymbol{\mu}_B \quad \dots \quad \boldsymbol{\mu}_B)$$

Then, we compute the singular value decomposition

(B8) $$\mathbf{UEV}^T = (\mathbf{A} - \mathbf{M}_A)(\mathbf{B} - \mathbf{M}_B)^T$$

The least-squares solution for the rotation matrix $\mathbf{R}$ is given by

(B9) $$\hat{\mathbf{R}} = \mathbf{VU}^T$$

Once we compute the least squares solution for $\mathbf{R}$ we can estimate the translation component of the rigid-body transformation by inserting $\mathbf{M}_A$ and $\mathbf{M}_B$ into eq. (B1) and solving for $\mathbf{T}$

(B10) $$\hat{\mathbf{T}} = \mathbf{M}_B - \hat{\mathbf{R}}\mathbf{M}_A$$

Reference

Arun, K. S., Huang, T. S., and Blostein, S. D.. 1987. Least-squares fitting of two 3-D point sets. IEEE Trans. Pattern Anal. Mach. Intell. (5): 698–700.

J. Unmanned Veh. Sys. Downloaded from cdnsciencepub.com by Thomas Rapstine on 12/16/21
For personal use only.